Correlating structural and electrical characteristics of threading dislocations in GaN-on-Si heterostructures and *p-n* diodes by multiple microscopy techniques

Albert Minj[1,], Karen Geens[1], Hu Liang[1], Han Han[1], Céline Noël[1], Benoit Bakeroot[1,2], Kristof Paredis[1], Ming Zhao[1], Thomas Hantschel[1], Stefaan Decoutere[1]*

[1]IMEC, Kapeldreef 75, Leuven 3001, Belgium

[2]CMST, Ghent University, Technologiepark 126, 9052 Gent, Belgium

(Receipt date: 30/03/2022)

*albert.minj@imec.be

Abstract

Structural and electrical properties of *a*- and *a*+*c*-type threading dislocations in metal organic vapor phase epitaxy grown Si-doped GaN (0001) were determined by combining multiple scanning probe microscopy approaches. The analysis examines the space charge region (SCR) formed around dislocation cores and clarifies the role it plays in influencing the local recombination, the surface potential characteristic and even the conductivity. The direct evidence of the SCR was obtained from a differential capacitance (d*C*/d*V*) measurement at dislocation sites on the (0001) surface. Experimental d*C*/d*V* (V) measurement results supported by Technology Computer-Aided Design calculations of capacitance accounting for the theoretical deep levels related to different atom core-structures of the identified dislocations revealed quantitative differences in their respective trap densities. This study was extended to *p*-*n* GaN vertical diodes to analyze doping distribution across the active layers. Through a correlated cross-sectional investigation combining electron channeling contrast imaging microscopy, the underlying dislocations within the depth limited by the screening of their SCRs were found to severely impact the homogeneity of the cross-sectional d*C*/d*V* contrast in the low-doped *n*-type drift layer of the diodes. This raises serious concern regarding any quantification effort by differential capacitance measurements in GaN-on-Si, where the dislocation density is in the order of 10^9 cm^{-2}.

I. INTRODUCTION

Energy efficient III-nitride power devices benefit from GaN's superior intrinsic properties that include a wide band gap, a high electron saturation velocity, and a high thermal conductivity [1]. Its compatibility with complementary metal-oxide-semiconductor technology and cost-effective fabrication on 6- and 8-inch Si substrates have attracted market attention for high-power and high-frequency GaN-on-Si devices which are already reaching 1.2 kV applications [2–4]. However, even today threading dislocations (TDs) on such substrates are still present in quantities reaching 10^9 cm^{-2}, nearly an order of magnitude higher in comparison to SiC and sapphire substrates. Hence, their electrical properties must be better understood for improved device design and simulation calibration. Since the 1990s, their electrical activity has been a subject of debate due to the incoherence of the findings obtained from different characterization techniques probing leakage, recombination, and charge state. This was partly attributed to a lack of a database of all stable atom-core structures and associated electronic structures. For example, techniques such as conductive-atomic force microscopy (C-AFM), which measures local current, prominently assigned leakage paths in *n*-type GaN to open-core screw-type dislocations [5–8], and also to full-core and mix-type dislocations [5,6]. Emission microscopy analysis in GaN *p*-*n* diodes, on the other hand, associates them solely to full-core screw dislocations [9,10] while claiming nanopipes (or open-core structures) to be electrically inactive [11]. In regards to their recombination properties, authors in references [12–15] determined the other types of TDs , mainly edge- and mixed-types, as non-radiative recombination centers using cathodoluminescence (CL) microscopy. Optical technique, confocal microscopy, employing two-photon excitation with below band gap wavelengths corroborated their non-radiative nature along the dislocation length, although with a diffraction-limited resolution [16]. Kaganer et al. pointed out that exciton

dissociation is likely to occur in the sub-surface region around TDs with an edge character due to the polarization-induced field (or charges) at the (0001) surface termination [17]. Despite being non-radiative in nature, this form of recombination differs from Shockley-Read-Hall recombination, where traps play a critical role. Therefore, further knowledge of the charge state or charge-induced field at TDs can be crucial for understanding the recombination dynamics in the bulk. Using electron holography, Cherns et al. determined the line charge density of edge-type TDs, but from such an analysis shallow or deep nature of traps cannot be implicated [18]. They also pointed out the difficulties in extending this study to mixed- and screw-type dislocations due to the influence of surface relaxation associated with the screw component. Besides, microscopic defects formed during sample preparation (e.g., ion milling) for such an analysis had not been considered for charge quantification. Overcoming these limitations and the challenge associated with making statistical analysis, Simpkins et al. revealed that both edge- and mixed-type dislocations are negatively charged in as-grown *n*-type GaN buffers by assessing the surface potential build-up around them using Kelvin probe force microscopy (KPFM) [19]. Similar KPFM-based study was later extended to InGaN alloys [20]. In these studies, surface potential variation corresponding to only few tens of millivolts has been observed at charged dislocation sites. Another non-destructive technique involving differential capacitance (dC/dV) measurements is scanning capacitance microscopy (SCM) which can also reveal space charge regions around dislocations [21–23]. Unfortunately, neither a quantitative dependence of surface potential values on local charges at TDs was made (or vice versa) nor a dC/dV analysis led to the quantitative determination of a dislocation-related parameter.

Furthermore, this kind of an in-depth analysis of TDs is highly desired in a fully fabricated *p*-*n* diode, where access to the lightly doped *n*-type drift layer is prohibited by the overgrown layers

(highly doped *p*-type layer, *n*+ layer, metallic contacts, and passivation layer). As the entire GaN stack undergoes multiple treatments such as high-temperature annealing steps (Mg-activation, ohmic contacts, passivation, etc.), the availability of an investigative methodology to monitor the alteration in the electrical characteristics of TDs can be decisive. In this regard, the method employed by Ebert et al. to probe TDs through non-polar cleavage planes has been adopted in this work as a solution to this problem [24,25].

The discrepancy stated above over electrical properties of TDs partly arises from assuming their dependence on the Burgers vector ***b*** rather than on their core structure. Even though several core structures can exist for the same ***b***, the electronic properties are strictly defined by the core structures, which depend on the growth stoichiometry, and can be altered during device processing steps. Our study clarifies how the space charge at TDs in Si-doped GaN correlates to local recombination, surface potential, and conductivity characteristics. It elaborates a methodology based on the analysis of dC/dV (V) via computational effort to confirm their deep acceptor nature (i.e., energy levels in the mid-gap and below) and to extract the trap density without inducing damage to the sample. For the extracted occupied trap density, typically measured small surface potential values across dislocations in KPFM can be justified. Eventually, the nature of their electrical behavior can be reliably associated with identified core-structures of the most statistically dominant TDs, namely edge- and mixed-type.

II. EXPERIMENTAL SECTION

A. Description of the samples

Three types of semi-vertical GaN *p-n* diodes, which differed primarily by the structural characteristics of their *n*-GaN drift layers, were investigated on their cross-sections by scanning

probe microscopy (SPM). The GaN epitaxial stacks were grown by metal-organic chemical vapor deposition (MOCVD) on 200 mm substrates, where for two of them (samples A-Si and B-Si) Si (111) substrates and for the third one (sample C-QST) Qromis Substrate Technology (QST®) substrate were used [26]. The QST substrate is an engineered wafer with poly-AlN core and a conductive monocrystalline Si(111) layer at the frontside, on top of a buried oxide. All the active layers of the diode, *p*-type, *n*-type, and *n*+ layers, were separated from the substrate by a 1 µm thick *u*-GaN buffer and strain management layers (SMLs). Both samples A-Si and B-Si consisted of a stack with a limited drift layer thickness of 750 nm and with a Si doping concentration of $3x10^{16}$ cm^{-3} and $1x10^{17}$ cm^{-3}, respectively, while sample C-QST had a 3 µm thick drift layer with a Si doping of $4x10^{16}$ cm^{-3}. The GaN stacks were terminated by an *n*+ layer, right above the *p*-type layer, which was etched off during the post-growth processing of the diode structure. The description of the drift layers in the three samples are summarized in table 1. The complete structural details of the as-grown stack on Si substrates and the processed diodes are schematically shown in Figure 1(a). Nominal values of Si and Mg concentration were determined by secondary ion mass spectrometry (SIMS) on as-grown stacks. Cross-sectional electrical measurements were carried out on the cleaved plane (11-20) under the *p*-contact (cathode) of the fully fabricated devices, where both cathode and anode electrodes were accessible from the top. The cleaving was done in ambient conditions. The active area of the *p*-*n* diode under study is ~ 100x100 μm^2. A fourth sample, D-Si, consisting of a 1.7 µm thick *n*-GaN layer with Si doping of ~$4x10^{16}$ (similar to that of the drift layer in A-Si) grown on a AlGaN/AlN buffer on Si, was used for plane-view investigation emulating a common SPM approach.

Sample	**Drift layer**		**Substrate**
	Thickness (nm)	Doping concentration (cm^{-3})	
A-Si	750	$3x10^{16}$	Si
B-Si	750	$1x10^{17}$	Si

C-QST	3000	$4x10^{16}$	QST®

Table 1: Description of the drift layers in the three samples consisting of *p*-*n* junction that were used for cross-sectional investigation.

B. Methodology

The SCM analysis was done on a Park Systems NX-Hivac tool on the sample cross-sections prepared both by cleaving and by chemical mechanical polishing (CMP) and on the as-grown surface. For cross-sectional analysis, an AC bias in the range of 0.25 – 3 V at 17 kHz was used to obtain the d*C*/d*V* amplitude (or | d*C*/d*V* |) and phase maps across the GaN stack under the *p*-contact electrode and for the planar analysis on the (0001) *n*-GaN surface, 5 V was used. d*C*/d*V* versus bias curves (or d*C*/d*V* spectroscopy) acquired locally were also analyzed by sweeping the sample DC bias within the ±5 V limit. The following scheme for the bias sweep was used in every spectroscopy; 0 V → maximum positive bias → minimum negative bias → 0 V, with a total acquisition time of 5 s. Further details of the SCM setup are described in Ref. [27]. KPFM measurements were carried out in the same tool in the side-band frequency modulation mode with an applied AC bias of 1.5 V at 2.5 kHz at a tip-sample separation of approximately 10-12 nm. Pt/Ir coated Si cantilevers with nominal spring constant (resonance frequency) of 7.4 N/m (150 kHz) and 2.8 N/m (75 kHz) were used for KPFM and SCM measurements, respectively. C-AFM measurements were made using in-house highly doped full diamond tips (spring constant ~ 3 N/m).

Electron channeling contrast imaging (ECCI) and cathodoluminescence (CL) imaging were executed on a Thermo Fisher Scientific Apreo SEM system equipped with a retractable solid-state backscattered electron detector and a retractable RGB CL detector. The former was used to localize the crystalline defects both in the cross-sectional view of the *p*-*n* diodes and in the planar-view of the as-grown *n*-GaN (0001) surface, while the latter was implemented to investigate local

recombination properties. ECCI was carried out at an accelerating voltage (AV) of 5 kV with a beam current (I_{beam}) of 0.8 nA at a working distance (WD) of 5 mm. Detailed information on the experimental setup can be found in Ref. [28]. As the electron channeling contrast can be affected by strong morphological changes, the cleaved cross-sectional device surface was smoothened out by CMP. To avoid the influence of carbon contaminations, introduced by the electron beam during ECCI measurement on the SCM analysis, SCM was carried out prior to ECCI to ensure that the correlative investigation using the two methods can be conducted. The CL imaging conditions were AV = 7 kV, I_{beam} = 0.8 nA and WD = 7.0 mm. The panchromatic CL imaging mode is used, which collects the emitted light with a wavelength ranging from 300 to 1100 nm.

III. RESULTS AND DISCUSSIONS

A. Cross-sectional study of *p-n* diodes

Figure 1 (b,c) shows an overview of the SCM analysis of sample A-Si and B-Si. Under the lock-in amplifier configuration, d*C*/d*V* phase maps consistently reveal *p*-type and *n*-type regions in the Si reference samples at phases of ~ 30 degrees and ~ -150 degrees respectively. This relation of absolute phase value to doping type allows us to identify the Mg-doped region as *p*-type and all the three Si-doped layers (drift layer, two degenerately doped *n*+ layers) as *n*-type in all the GaN epitaxial stacks under investigation. The two oppositely doped regions are easily deducible from the black and white contrast regions in the phase map (Fig. 1b, shown only for A-Si). The absolute phase values can be seen in the phase profile obtained across the stack in Fig. 1c. In the *n*+ layers and in the *p*-GaN layer, the |d*C*/d*V*| strength is much lower than in the drift layer, which is well aligned with the work of Lamhamdi et al. [29], who conducted a similar analysis on semi-vertical GaN stacks grown on an Al_2O_3 substrate. This can be understood from the dependence of |d*C*/d*V*|

on the carrier density as described in the numerical calculations by Giannazzo et al. [30], where the $|dC/dV|$ monotonously decreases with the carrier density exceeding 10^{16} cm^{-3}. This trend was also confirmed in the experimental work by Sumner et al. for a doping concentration higher than 10^{17} cm^{-3} [31]. The phase contrast in the 1 µm thick region consisting of the *u*-GaN buffer and the SMLs appears with a seamless texture noise effect contrast, which is due to a negligible signal strength. This implies that the carrier density in the unintentionally doped buffer layer is much lower than 10^{14} cm^{-3}, an upper limit determined for the lowly doped region of the imec calibration Si sample T8/3 [32] for the RF resonant capacitance sensor used (see Figure S1 in the Supplemental Material [33]).

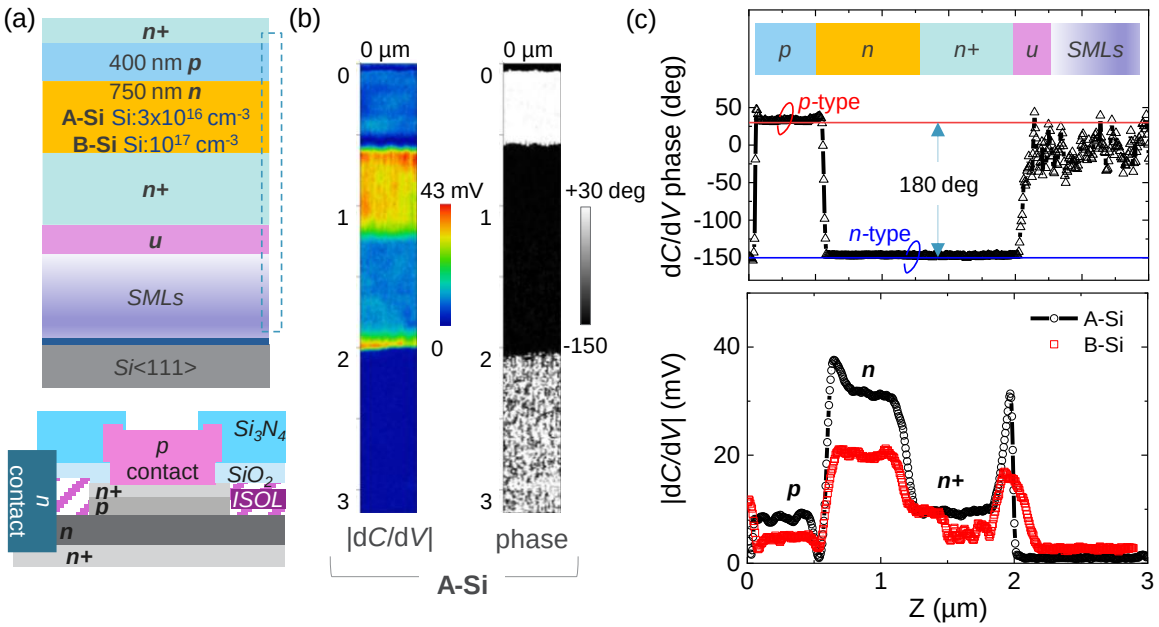

Figure 1: (a) Schematic of the structural detail of the as-grown GaN-on-Si stack (above) used in the semi-vertical *p-n* diodes, sample A-Si and B-Si (below). (b) Local $|dC/dV|$ and phase maps obtained in SCM analysis on A-Si at AC bias = 2.5 V. (c) Extracted and averaged $|dC/dV|$ and phase profiles across the semi-vertical diodes for A-Si (in black) and B-Si (in red). Phase value of

~ -150 degrees corresponds to all electron-dominated regions and ~30 degrees to hole-dominated regions.

The d*C*/d*V* spectroscopies obtained over multiple points (1 spectroscopy per 40 nm along the growth direction) across the *p*-*n* junction are shown in figure 2a. The formation of the peak (typically seen here for negative biases) is indicative of the typical high-frequency capacitance-voltage relation for an *n*-type MOS structure, which is formed here by the metallic Pt/Ir tip, native oxide and GaN. As the acquisition progresses from the region in the bulk of *n*+ GaN to *n*-GaN and then towards the *p*-*n* junction, a distinct trend can be seen in the progression of the spectroscopies. The magnitude of the |d*C*/d*V*| peak is initially small in the *n*+ region (positions 1 to 7 in Figure 2b) but can be seen increasing drastically as one approaches and enters the *n*-GaN layer (positions 8 to 10). Then, within the bulk of the *n*-GaN drift layer region, all the d*C*/d*V* curves almost overlap with each other (positions 9 to 22), which indicates homogeneity in the electron density along the growth direction in this layer. However, near the *p*-*n* junction, this trend interrupts and the peak magnitude increases monotonically within 80 nm in the Si-doped side. Typically, the dependence of |d*C*/d*V*| on doping concentration is not entirely monotonic over a broad range of concentrations (~10^{12} cm^{-3} to ~10^{20} cm^{-3}). When starting from a very low carrier density, |d*C*/d*V*| tends to increase with the carrier density reaching a maximum at n_{max} and then monotonically reduces with a further increase in the carrier density. From the computation by Giannazzo et al. [30] this value appears to be below 1x10^{16} cm^{-3}. Our Synopsys technology computer-aided design (TCAD) simulation (see Figure 2c) shows that while approaching the *p*-*n* junction the electron density drops from ~3.3x10^{16} cm^{-3} (close to the bulk *n*-GaN density) to ~9.6x10^{15} cm^{-3} within ~80 nm. This spatial extent coincides well with the drastic increase of |d*C*/d*V*| peak observed between position 22 and

24. As one moves further 40 nm towards the metallurgical junction, the calculated electron density drops to ~1.3×10^{15} cm^{-3}, which is accompanied with the lowering of the $|dC/dV|$ peak (position 25) indicating that the concentration surpasses n_{max}. This suggests that n_{max} is somewhere between 10^{15} cm^{-3} to 10^{16} cm^{-3} for GaN. Using the experimental $|dC/dV|$ peak magnitude across the *p*-*n*/*n*+ layers and analyzing it against the corresponding calculated bulk electron density (Figure 2c), a non-monotonic dependence could be envisaged (see Figure 2d). The data points related to *n*/*n*+ are scattered outside this monotonic dependence, which is possibly related to a sharp decline in the carrier density from the *n*+ to *n*- region and a poor SCM resolution. From position 25 onwards, a non-negligible $|dC/dV|$ is seen for positive biases (1.5 V – 2.5 V) which indicates that the net capacitance is influenced by the space charge region of the adjacent *p*-type region as well. A similar duality of the tip-sample capacitance sensitivity to the space charge regions of both *n*-type and *p*-type regions has been previously reported for Si *p*-*n* junctions [34]. In the bulk of the *p*-GaN layer, where the calculated hole density for the given Mg concentration is ~ 9.4×10^{17} cm^{-3}, the SCM signal strength is expected to be small. As one further approaches towards and into the *p*-type region, the $|dC/dV|$ component of the *n*-type region recedes and disappears (position 25 to 27), while the component of the *p*-type region remains almost unchanged in the positive bias range. In positions from 28 to 35, which corresponds to the bulk of *p*-GaN layer, the $|dC/dV|$ is completely screened from the junction within the given bias range. As seen in the $|dC/dV|$ map, we also consistently observe an unusual increment in $|dC/dV|$ near the *n*+ GaN/*u*-GaN interface despite low $|dC/dV|$ in the two adjacent layers. This can be simply explained by the carrier diffusion (electrons in this case) from the *n*+ layer into the *u*-GaN layer, thus locally reducing the electron density in the *n*+ layer while enhancing the electron density in the *u*-GaN buffer near the interface. Even though, the $|dC/dV|$ contrast analysis up to this point is in line with the work of Lamhamdi et

al. [29], a significant difference in the homogeneity of the |d*C*/d*V*| distribution in the drift layer can be seen at a larger scale. This is due to the threading dislocation density, which is one order of magnitude higher in GaN-on-Si stacks used in this investigation and is explained next.

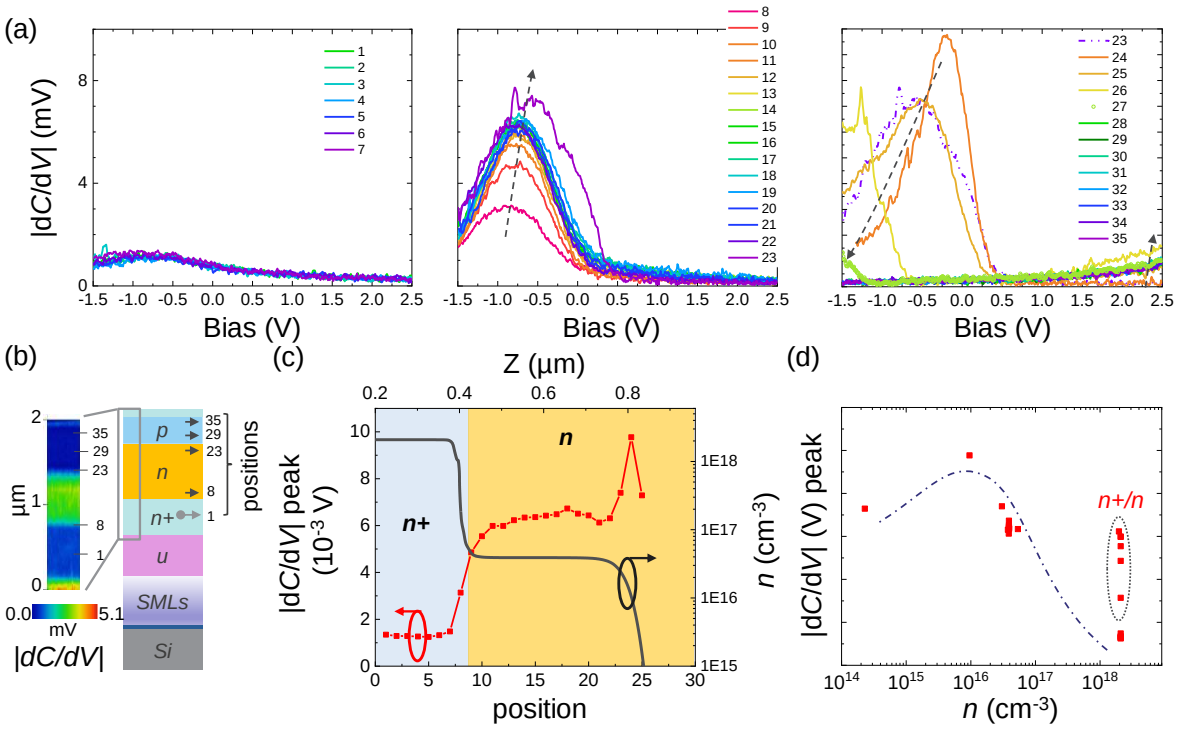

Figure 2: (a) |d*C*/d*V*| spectroscopies at discrete positions, 1 – 35, across the cleaved cross-section of A-Si. (b) Positions 1-35 schematically shown correspond to indicated locations in the stack and on the |d*C*/d*V*| map. (c) Trend of |d*C*/d*V*| peak and calculated electron density between position 0 (in *n*+ bulk) and position 25 (in *p*-*n* space charge region) or equivalently between 0.20 and 0.96 μm (top horizontal axis). (d) Non-monotonic dependence of |d*C*/d*V*| on electron density extracted from the calculated n profile and experimental |d*C*/d*V*| profile across the GaN stack.

|d*C*/d*V*| contrast formation in the drift layer was notable in the larger scan size (> 3x3 μm^2) in the drift layer. This is shown for both Si substrate-based samples and the one on the engineered

QST® substrate in Figure 3. For sample A-Si, the |dC/dV| distribution was non-uniform in the drift layer with a Si doping of ~3x10^{16} cm^{-3}. Here, the contrast is formed by the appearance of skewed-funnel type local features representing a significant drop in |dC/dV| and it extended across the drift layer. We verified that there were no hints of similar features in the topography (indicated with a dashed curve), thus ruled them out as a morphology-induced artifact. Interestingly, this contrast characteristic was less evident for sample B-Si where the Si doping (~1x10^{17} cm^{-3}) was ~3.3 times higher. Usually, a diminishing |dC/dV| is associated with the presence of a depletion /space charge region (which is why at the *p*-*n* electrical junction |dC/dV|→ 0) or high metallicity. Here, for low doping concentration in the drift layer, diminishing |dC/dV| around a dislocation strongly suggests that it is surrounded by a larger depletion region (equivalently a smaller capacitance). One may expect the local Mg diffusion from the *p*-GaN layer into the drift layer to result in the formation of a local junction within the drift layer. Although Mg diffusion into the drift layer as evidenced by TOF-SIMS technique (see depth-dependent chemical analysis of the Mg-dopant in Figure S2 the Supplemental Material [33]) is highly exaggerated by the bombardment of primary ions, it is identical within the two samples. Despite this, the local depletion regions were less evident in B-Si in the SCM analysis. Therefore, the contrast seen for low doping concentration is less likely to relate to Mg diffusion. In sample C-QST with a thicker drift layer (~3 μm) and a Si doping (~4x10^{16} cm^{-3}) similar to sample A-Si, the |dC/dV| spatial distribution also included skewed-funnel type features with a diminished signal strength (see Figure 3c). Due to a larger thickness of the drift layer, the tail of these features can be fully seen extending across the drift layer to the underlying *n*+ GaN layer. This extended tail-like feature, therefore, could be attributed to those threading dislocations, which are usually encountered in a GaN stack. The formation of a funnel-type contrast can be understood from the conjunction of space charge regions of the *p*-*n* junction and

around the dislocation. This is clearly seen in the TCAD simulation of a dislocation (see Figure 4) along a *p*-*n*/*n*+ diode structure where the calculated space charge density around the dislocation reaches $4x10^{16}$ cm^{-3}. The simulation was done using the parameters given in Ref. [35]. Equivalently, one may also interpret that this region is fully depleted i.e., with negligible electron density and therefore, it would result in a d*C*/d*V* signal close to noise level.

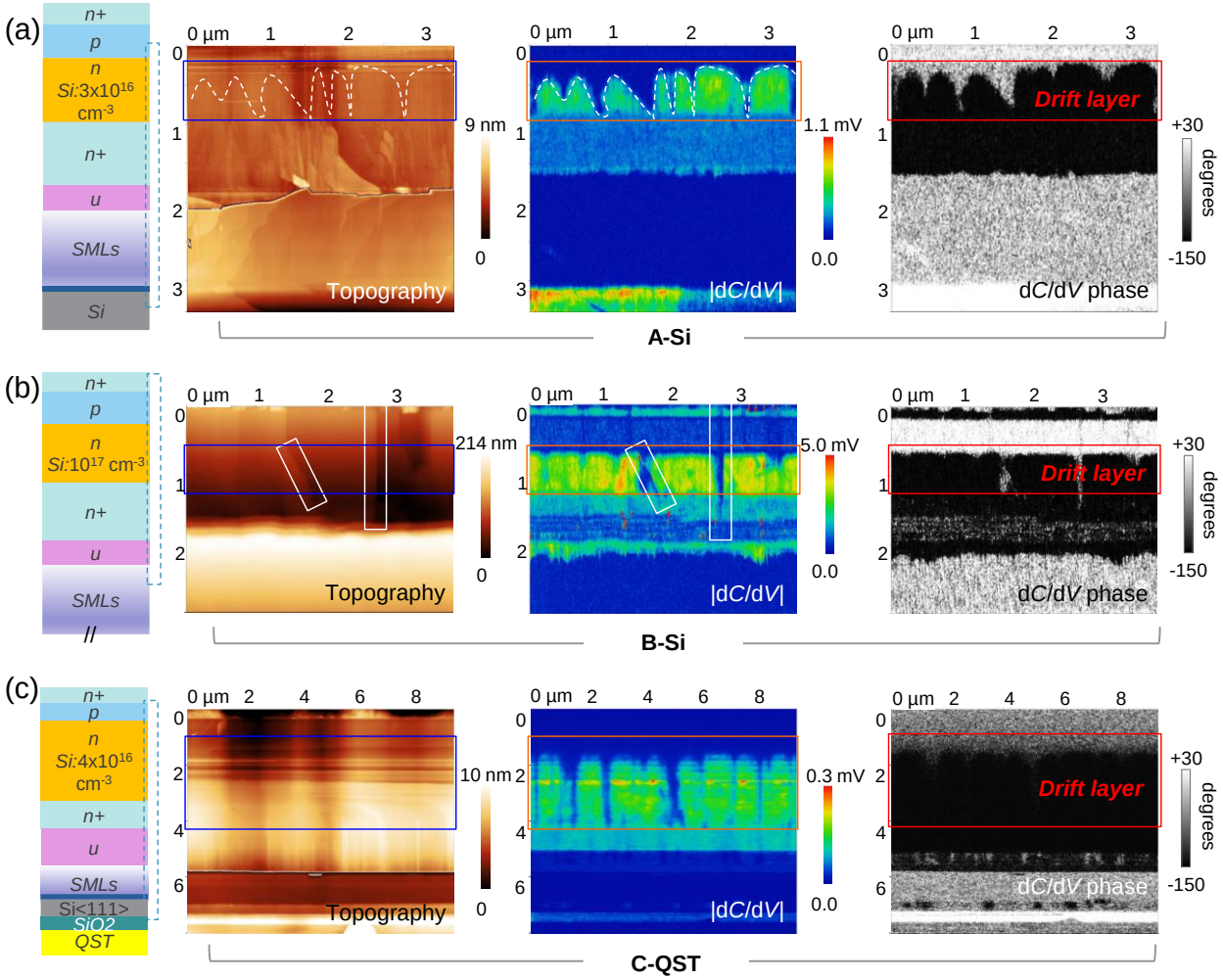

Figure 3: Simultaneously acquired morphologies, |d*C*/d*V*| and phase maps for (a) sample A-Si at 1 V AC bias, (b) B-Si at 1 V AC bias and (c) C-QST at 0.5 V AC. DC bias = -0.5 V and the lock-

in frequency is fixed at 17 kHz in (a)-(c). Morphology related artifacts in the |d*C*/d*V*| map are enclosed in white boxes in (b).

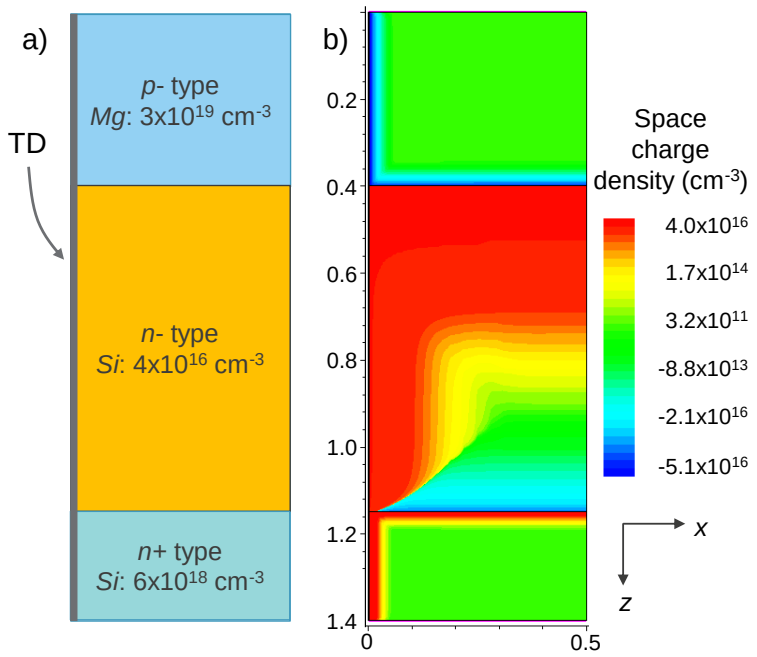

Figure 4: (a) Schematic of the structure used in the simulation of a dislocation (located at the left edge, $x = 0$) across *p*-*n*/*n*+ diode (1.4 µm x 0.5 µm) and the calculated (b) space charge density.

In order to confirm our hypothesis that the contrast formation in |d*C*/d*V*| maps can be attributed to TDs with high certainty, ECCI was carried out on the CMP prepared cross-section of one such device. Contrast in ECCI is generated by the intensity change of backscattered electrons due to small disturbances in atomic planes around extended defects (e.g., dislocations and stacking faults). In the ECCI micrograph (Figure 5a), the comet-like features along the growth direction can be observed. They are accompanied with dark dots indicating the dislocation termination on the CMP prepared non-polar surface. This is because threading dislocations are not always perfectly aligned either along the [0001] direction or parallel to the CMP prepared cross-sections.

In addition, CMP also introduced some curvature in the surface. Routine SCM analysis was carried out on this very same area and the |d*C*/d*V*| maps also feature a funnel-like contrast due to the diminished signal. Such features are found exactly at the locations of dislocations identified in the ECCI analysis (Figure 5b). Thus, this confirms a strong association of local depletion regions around threading dislocations. It also explains why such contrast was not observed in a similar study by Lamhamdi et al. [29] as their GaN stacks were grown on an Al_2O_3 (0001) substrate, which had a ~ 10x lower TD density.

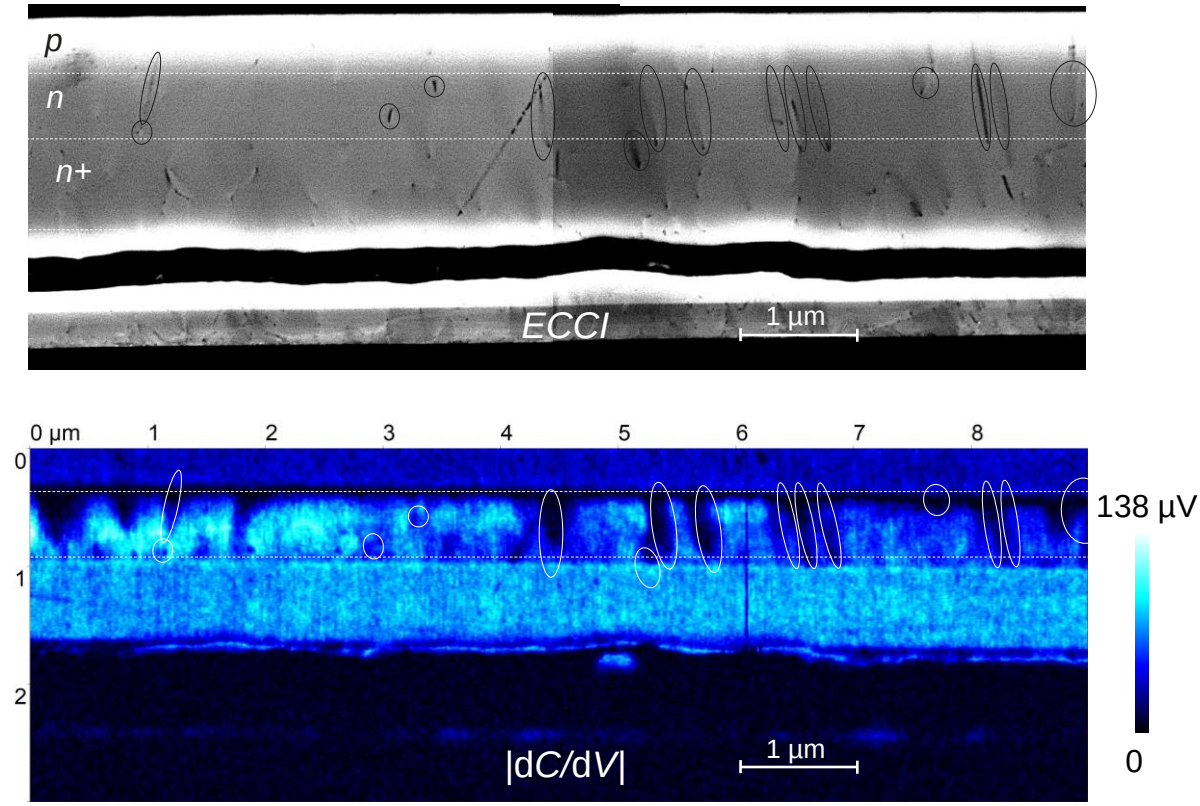

Figure 5: (a) ECCI and (b) |d*C*/d*V*| map at AC bias of 1 V at 17 kHz on the same area of CMP prepared cross-section of B-Si.

In order to understand why the contrast related to the depletion region around the threading dislocations was not evident in cleaved cross-section of sample B-Si, one can refer to the work of

Baghani et al. on the screening of charged dislocations by background electron carriers [36]. They calculated the space charge density profile around dislocations acting as deep acceptors (charged at 1e/unit cell) in GaN, which shows a significant screening of charged dislocations as the background carrier density goes from 10^{16} cm^{-3} to 10^{17} cm^{-3}. Correspondingly, the fully depleted radius reduces from ~150 nm to ~50 nm, whereas, for a higher concentration in the order of 10^{18} and 10^{19} cm^{-3}, fully depleted radii can reach values lower than 10 nm [36,37]. Because of the poor screening for a low carrier density, the capacitance formed by the depletion region of the dislocations adds to the tip-sample junction capacitance in series, thereby reducing the net capacitance and consequently, the $|dC/dV|$. It is for an improved screening by carriers that the local regions with dislocation induced $|dC/dV|$ drop appear with a much lower density on CMP prepared cross-section of B-Si (Figure 5b) when compared to the one on the cleaved cross-section of A-Si (Figure 3a). It is expected that the contrast formed by dislocations in B-Si are located close to the surface, where background carriers are fewer in density. The capacitive behavior of the depletion region can also be further corroborated from the bias dependence of the net capacitance (or net dC/dV) in SCM analysis. As explained earlier in the spectroscopy analysis in Figure 2, the forward bias regime in the *n*-type (*p*-type) region is seen for negative (positive) voltages applied to the sample, while the reverse bias regime is for the opposite polarity of this voltage. At a DC bias of 0 V, dislocation-related tail features can be seen running across the drift layer in the $|dC/dV|$ map (see Figure 6a). But as one goes into the forward bias regime (i.e.-0.5 V), the space charge region around the dislocations shrinks, thereby narrowing the lateral width of the tail-like features in the $|dC/dV|$ map and improving the sharpness of such features (see Figure 6b). Interestingly, at this bias condition, tail-like features can be seen extending into the undoped GaN buffer, which was

not visible at the 0 V bias condition. In the next section, electrically active TDs are identified and their role as recombination centers is discussed.

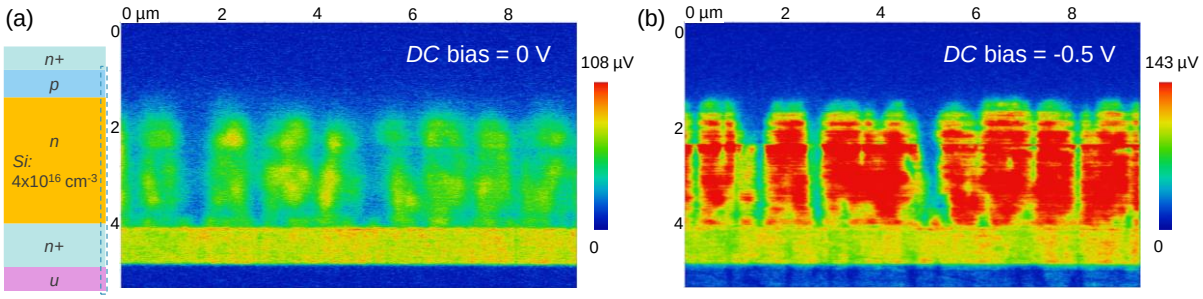

Figure 6: |d*C*/d*V*| acquired in a single scan measurement (a) at DC bias = 0 V and (b) at -0.5 V using trace and retrace directions of the scan, respectively. The measurement area is indicated in the schematic of the stack in (a). Note that (b) corresponds to Figure 3(c) but in order to emphasize the dislocation related contrast also in the *n*+ and undoped GaN buffer, its color contrast is saturated by clipping the maximum signal strength to 143 µV.

B. Investigation of TDs in *n*-GaN(0001): space charge, recombination, surface potential and leakage paths

I. Space charge and leakage analysis

Further analysis to investigate any distinction in electrical properties or potentially the depletion behavior around dislocations owing to their structural type, *a*- (pure edge), *c*- (pure screw) or *a*+*c*- (mixed), was also conducted. As it was not feasible for us to identify the type of dislocations by ECCI neither on the cross-section nor on the (0001) surface because of the limited field of view, a morphological analysis of the (0001) surface of a 1.7 µm-thick *n*-GaN layer was instead relied upon. Here, the *n*-GaN layer was Si doped with ~4x10^{16} cm^{-3}, similar to that in the drift layer of A-Si. A transmission electron microscopy analysis using diffraction vectors <11-20> and <2-1-

11> estimated the pure-screw dislocations to be 3-5% of the total dislocation density. The morphology of the as-grown (0001) surface exhibited well-known step-terrace features and pits with two distinct characteristics (see Figure 7a). *a*+*c*-type dislocations, because they possess the *c*-component, tend to terminate the terraces and open in the form of pits, while the *a*-type ones do not interact with the terraces and terminate at the surface with minimal effect on the morphology. It is evident in the SCM analysis (see Figure 7b) that |d*C*/d*V*| tends to reduce around both *a*-type and *a*+*c*-type TDs but with different strengths. The comparison of |d*C*/d*V*| profiles across both types of dislocations is shown in Figure 7c. Although it is subtle, this difference can be seen. As explained earlier in the cross-sectional study, a diminished |d*C*/d*V*| indicates the presence of a space charge region around the dislocations. As |d*C*/d*V*| diminishes more severely at *a*-type TDs, it implies that the space charge induced around their negatively charged core is more prominent than at *a*+*c*-type dislocations. This is determined by the position of the unoccupied states in the forbidden gap at the dislocation core, their density of states and occupation probability, which comes down to the atomic arrangement of the core. As these dislocations can be associated with deep level states and it is the mid-gap states rather than shallow states that can result in non-radiative recombination, a recombination assessment was further investigated using CL and is discussed in detail in the next section. The root cause of why |d*C*/d*V*| diminishes profoundly around *a*-type TDs requires complete structural analysis of the core and its surroundings. Our results, however, confirm that both types of dislocations are electrically active as inferred in Refs. [13,15].

The characteristic of the space region around *a*-type TD was further comprehended from the acquired d*C*/d*V* spectroscopy. This is shown in Figure 7(d) alongside the reference d*C*/d*V*(V) of a dislocation-free zone. As expected in the reference area, the d*C*/d*V* increases in the forward bias with reducing surface depletion width. At the *a*-type TD, the onset of d*C*/d*V*(V) is shifted by ~1.76

V with respect to the reference area. The net capacitance sensed under the tip at the *a*-type TDs is due to the space charge region of the dislocation which extends radially as well as along the dislocation across the entire *n*-GaN layer. Therefore, the local capacitance at the TD is negligible at 0 V. As the tip-sample junction goes under forward bias, the depletion region at the dislocation shrinks, increasing the local capacitance only gradually initially. It is not until the onset voltage (V_{th}) at ~ -1.57 V that the depletion region is narrow enough such that non-negligible dC/dV can be acquired. At this onset, the dC/dV (V) characteristic eventually becomes similar to that of the reference area at its respective onset voltage of ~0.19 V. The V_{th} is indicative of the junction potential due to a charged dislocation, which can be understood from the typical C(V) characteristic of a Schottky junction diode. The depletion width z_d and the resulting capacitance C at an applied bias V for such a junction is given by

$$z_d = \sqrt{\frac{2\epsilon_0\epsilon_{GaN}(\varphi_i - V)}{qN_d}} \text{ ... (1) and } C = \frac{A\epsilon_0\epsilon_{GaN}}{z_d} \text{ ... (2)}$$

where ϵ_{GaN} is the relative permittivity of GaN, N_d the doping density, φ_i, the electrostatic potential from band bending, A, the contact area, and q, the elementary charge, and ϵ_0, the vacuum permittivity. Further solving (1) and (2) yields

$$\frac{dC}{dV} \propto \frac{1}{(\varphi_i - V)^{3/2}} \text{ ... (3)}$$

As experimentally observed in the dC/dV spectroscopy, for $V \leq V_{th}$ at the dislocation and in the dislocation-free region,

$$\left.\frac{dC}{dV}\right|_{V \leq V_{th,TD}} \sim \left.\frac{dC}{dV}\right|_{V \leq V_{th,free}},$$

where $V = V_{th,TD}$ and $V = V_{th,free}$ stands for onset voltages at dislocation and dislocation-free region, respectively.

$$\Delta\varphi = \varphi_{i,TD} - \varphi_{i,free} \sim V_{th,TD} - V_{th,free} = 1.76V$$

The obtained $\Delta\varphi$ corresponds to a band bending of ~ 1.76 *e*V around the dislocation. However, it must be noted that the resulting $\Delta\varphi$ reflects the band bending in the sub-surface region rather than on the surface. Even though equation (3) can be applied to a tip-sample junction as if it were to behave as a planar capacitor without fringe effect or if it were a spherical capacitor (provided, tip contact area << depletion width), they should only be used here as an approximation. One will require numerical modelling to correctly extract the band bending from V_{th} shifts.

Similar to our observations, a diminishing $|dC/dV|$ signal strength and a similar magnitude of V_{th} shift were also reported by Hansen et al. [21] at the edge-type threading dislocation, though no distinction was made between *a*-type and *a*+*c*-type. In their dC/dV analysis, they only associated this shift to the presence of a positive charge around the dislocation. Here, for the *a*+*c*-type dislocations, the observed V_{th} shift was much smaller (~1.10 V) than for the *a*-type. This clearly indicates a significant difference in the electronic properties of these two types of dislocations with the *a*- component. Several computational investigations have shown that their electronic properties in terms of local density of states are closely linked to the structural configuration of their core. In scanning transmission electron microscopy analysis (see Figure S3 in the Supplemental Material [33]), the 5/7 atom-core structure was seen at *a*-type dislocations while both undissociated (5/6 double atom-core) and dissociated (5/7/4/8/9 atom-core) dislocations were observed for *a*+*c*-type dislocations. These findings are in good agreement with the work of Rhode et al. [38], who concluded that all *a*-type dislocations occur with the 5/7 core-structure and while the *a*+*c*-type can occur both as dissociated (5/6 double) and undissociated (5/7/4/8/9 and 5/7/4/8/9 core-atoms) in MOCVD grown Si doped GaN. DFT calculations by Belabbas et al. [39] predict deep acceptor states located ~ 1 *e*V from the valence band for both *a*-type TD with 5/6 atom-core and for undissociated *a*+*c*-type dislocations with 5/6 double atom-core structure. Unfortunately,

there are no theoretical studies available yet on the observed dissociated dislocations, but both our SCM contrast analysis and CL analysis suggest them to be deep acceptors. Since the V_{th} shift is clearly different for the two types of dislocations despite having the trap state around the same energy position, this can be understood in terms of difference in their electron trap density. We calculated a high frequency *C*-*V* characteristic of the nano-size metallic contact located on the top of the dislocation and on the free surface by TCAD simulation. Parameters relevant to the GaN/vacuum interface used here are discussed in the next section. An E_C-E_T of 2.5 *e*V was assigned for both types of dislocations, but the electron trap density was varied from 0.1 *e*/*u.c.* to 4 *e*/*u.c.* where *e*/*u.c.* is the electron traps per unit cell. As shown in the calculated |d*C*/d*V*| curves in figure 8(a), the experimental V_{th} shift of the *a*-type dislocation can be explained for a trap density of ~ 0.25 – 0.5 *e*/*u.c.*, while for the *a*+*c*-type dislocation, this is around 0.25 *e*/*u.c.* These dislocations were further investigated by C-AFM analysis for their contribution towards leakage path as it cannot be reliably inferred from SCM analysis alone. In figure 9, simultaneously acquired morphology and the C-AFM maps obtained at sample bias of -1.5 V are shown. The current magnitude drops significantly and preferentially around both *a*- and *a*+*c*-type dislocations. Some of these dislocations are also encircled. Since morphology change at *a*-type dislocations are minimal, they were not observable in topography obtained by the diamond tip but knowing that they exist as a bunch/chain from other microscopy techniques discussed above and allowed their identification in the current-map. It must be pointed out that the leakage or the current flow is suppressed by the potential barrier formed in the depletion region. C-AFM measurements were also carried out for the positive bias range up to +30 V but no current contrast was observed around dislocations. One must note that there was no sign of higher current at any dislocation considering up to 5% of the total dislocations could be pure-screw type. This observation is not in agreement

with the assertions made in the reports suggesting pure-screw type dislocations in *n*-GaN as leakage paths. On careful observations, such screw-type dislocations were associated with a V-shape opening [40], where work function and surface states of the semi-polar surfaces could play an important role in defining the local barrier height. In our case, we do not expect any notable differences in the surface morphology of mix-type and pure-screw dislocations. This scenario is also different from *n*-GaN [5–8] and Al(Ga,In)N/GaN heterostructures [41] where dislocations with screw component have been determined as the cause of leakage in heterostructures.

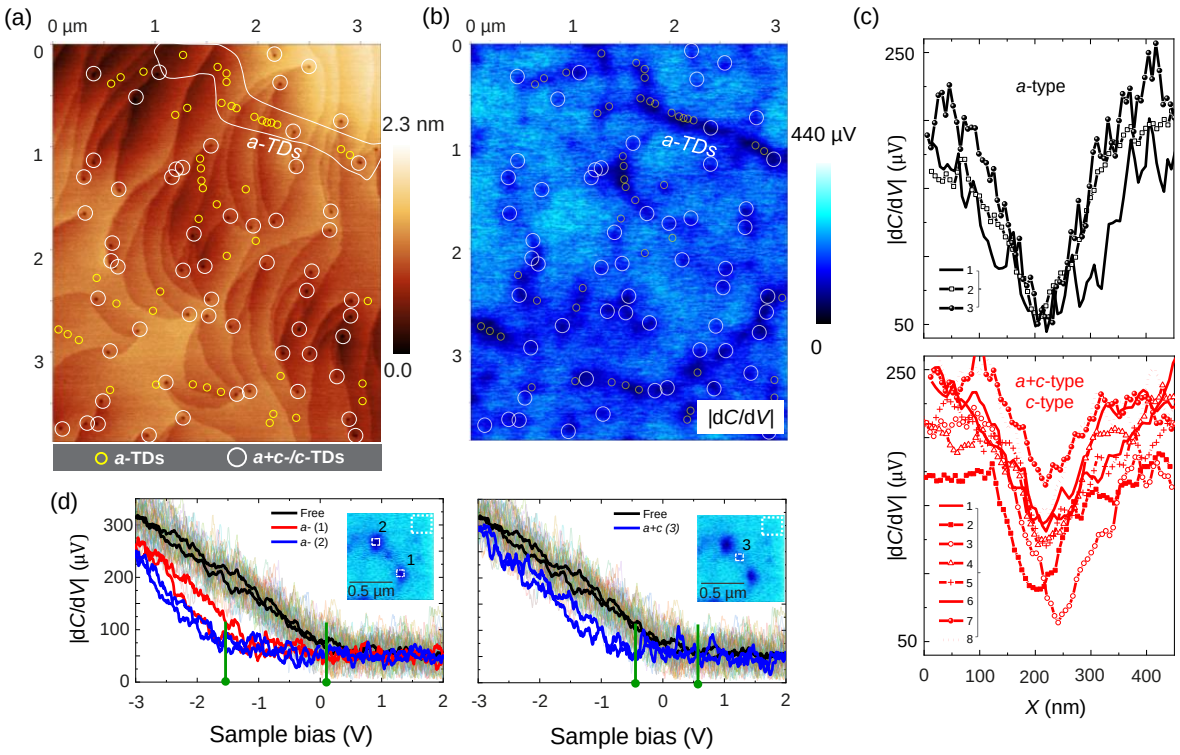

Figure 7: (a) Morphology and the corresponding (b) |d*C*/d*V*| at DC bias = -2 V. Line profiles of (c) |d*C*/d*V*| across three *a*-type and eight *a*+*c*-type or *c*- type TDs. The vertical scales are the same in the two graphs. (d) |d*C*/d*V*| spectroscopy at two *a*-type TDs (marked as 1, 2), at *a*+*c*-type TD (marked as 3) observed in the |d*C*/d*V*| map (inset) and in a dislocation-free region (averaged from

the box indicated in the inset), which is in black curve. The two vertical lines in green on the x-axis indicate the onset voltages V_{th}.

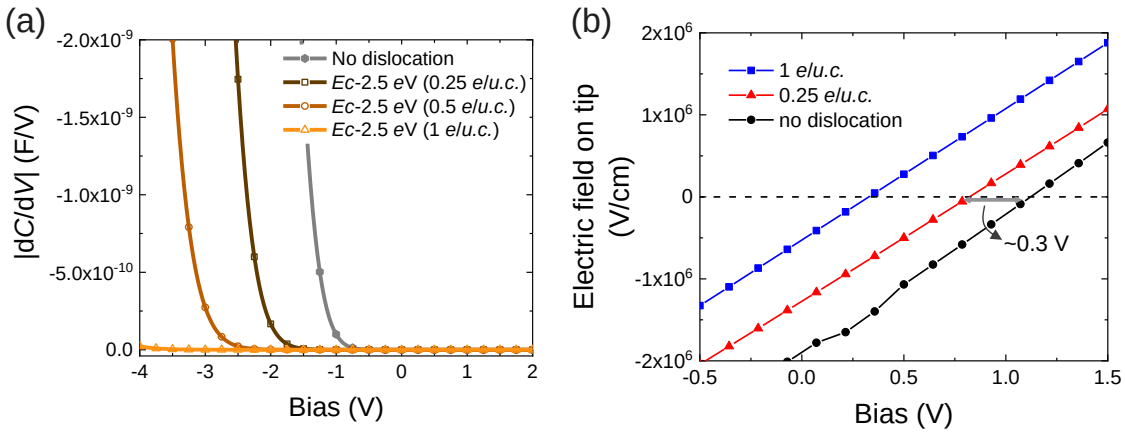

Figure 8: (a) Calculated |dC/dV| (V) of a metallic tip on a dislocation for varying defect level and electron trap density and dislocation-free region. (b) Calculated electric field (V) on metallic tip separated by 10 nm from the GaN (0001) surface with and without a dislocation.

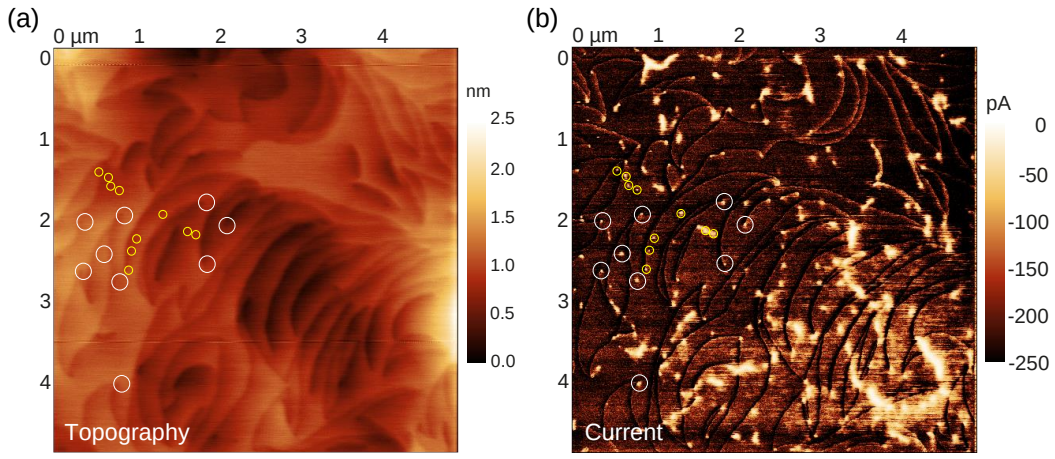

Figure 9: (a) Morphology and the corresponding (b) current map for a sample DC bias of -1.5 V. Some of the *a*+*c*-type and *a*-type dislocations are encircled in white and yellow, respectively, for the reader's aid.

II. Recombination analysis

The panchromatic CL micrograph acquired on this sample at 7 kV (see Figure 10b) is dominated by isolated dark spots and dark thread-like features, which are associated with severely diminished intensities. ECCI on the same area reveals that all *a*-type TDs are located at the thread-like structure, while the *a*+*c*-type can be found at the isolated spots (Figure 10a). Similar to the morphology analysis, ECCI was used here to identify the dislocation type based on their size and how they interact with the terrace-steps, which are also present in the micrograph. Our observations are in good agreement with other CL studies that report dark CL spots at all TDs, irrespective of their type as shown by Naresh-Kumar et al. [15], and for *a*- and *a*+*c*-type TDs shown by Albrecht et al. [13]. Even though it is generally understood that the dark spots in CL micrographs are due to local non-radiative recombination via electronic relaxation at dislocation-related traps, intrinsic polarization property of GaN can potentially affect how the recombination process occurs near the dislocation, even in the absence of traps. As *a*- and *a*+*c*-type TDs terminate at the (0001) surface, the discontinuity in the associated polarization results in bound charges forming high in-plane and out-of-plane piezoelectric fields in their vicinity. If the strengths of these fields are high enough, they can instantly dissociate the free excitons generated by the electron beam during the CL measurement and cause dark spots. Kaganer et al. [17] provided a simplified analytical expression for the electrostatic potential V(x,y,z) around such type of dislocations (located at the center of *x*-*y* plane along *z*) in GaN, from where the strength of the fields can be derived. V(x,z,z) is described as

$$V(x,y,z) = V_0 \frac{yz^2}{(x^2+y^2+z^2)^{3/2}} \quad \ldots (5)$$

where V_0 = 0.139 V, *x* and *y* are the in-plane axes and *z* is along the dislocation line parallel to [0001].

And the dissociation of exciton by the electric field is considered in terms of its characteristic dissociation time (τ_E), which is given by

$$\frac{1}{\tau_E} \propto \frac{1}{E} exp\left(-\frac{2E_0}{3E}\right) \ldots (6)$$

where E is the piezoelectric field and E_0 = 193 kV/cm is a factor dependent on the free exciton A binding energy, its reduced mass of exciton and the Bohr radius.

According to (6), τ_E monotonically decreases with the electric field, which means that a higher electric field facilitates a faster dissociation of an exciton. So, following the argument of Kaganer et al., one could roughly consider an E = 10 kV/cm as the cut-off field above which all excitons dissociate instantaneously as the equivalent τ_E ~0.12 ns from (6) is much smaller than the typical effective exciton lifetime in GaN [42,43]. Using (5) this cut-off field leads to a volume, which is enclosed radially within 70 nm from the dislocation and up to a depth of 140 nm from the surface. Any generated excitons within this volume should not contribute to the CL signals. The validity of 10 kV/cm as the cut-off electric field can be verified from the characteristic length of the dark spots in the CL analysis.

One factor that was not considered in their study, is the electric field of the typically present space charge region under the surface, even in the absence of a dislocation. To take this into account, a TCAD simulation of a dislocation across a GaN/vacuum interface was carried out. The parameters related to TDs used in this calculation are from Ref. [35]. Normally, in the absence of surface states, the calculated polarization induced field can be unrealistically high, therefore, surface donor traps were included in accordance with the experimental surface band bending [44]. The band bending was determined by analyzing the valence band spectra obtained from X-ray photoelectron spectroscopy, which revealed that the Fermi-level was located at ~ 2.61 *e*V above the valence band minimum near the surface (see Figure S4 in the Supplemental Material [33]) and

the bulk Fermi-level position is determined from the known value of free electron concentration. The surface donor trap density was accordingly tuned to bring the Fermi-level to lie at the experimentally determined position with a deviation of ~0.1 *e*V. The calculations reveal the existence of a sufficiently high electric field > 10 kV/cm up to the depth up of ~140 nm in the space charge region under the surface (Figure 11b,f), there will be no contribution to the CL signals. However, the Monte Carlo simulation, which does not account for the space charge region, shows that a moderate contribution to the CL generated (Figure 11f) from an electron beam energy of 7 k*e*V comes from a much lower depth up to ~240 nm. Therefore, the CL imaging contrast at 7 k*e*V mainly arises from the depth between z = 140 nm and z = 240 nm. Also, at these depths (Figure 11c,e), the in-plane electric field strength resulting solely from a charged dislocation (trap density ~ 1*e*/*u.c.*) is still high enough to dissociate excitons within a radius of 112±10 nm from the dislocation core. The observed full width at half maximum of the dark spot associated to an isolated dislocation in the CL map of ~ 218±102 nm is comparable to the calculated diameter (~224±20 nm) of the region enclosed within the boundary E = 10 kV/cm around a charged dislocation. Conversely, it also validates our assumption of 10 kV/cm as the cut-off electric field for exciton dissociation in GaN.

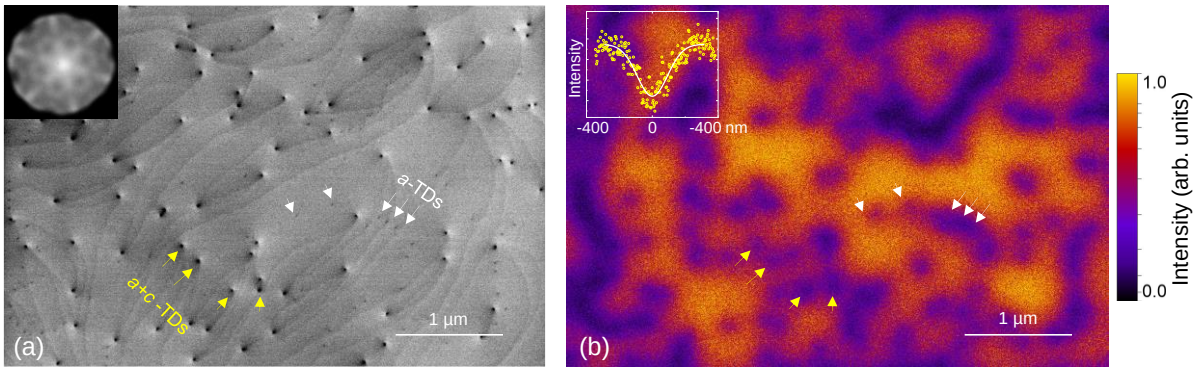

Figure 10: (a) ECCI micrograph at 5 kV and (b) panchromatic CL micrograph at 7 kV obtained on the same region. Electron channeling pattern and CL intensity line profile across an isolated TD are shown in the inset of (a) and (b), respectively. Some of the *a*- and *a*+*c*-type TDs are indicated by arrows.

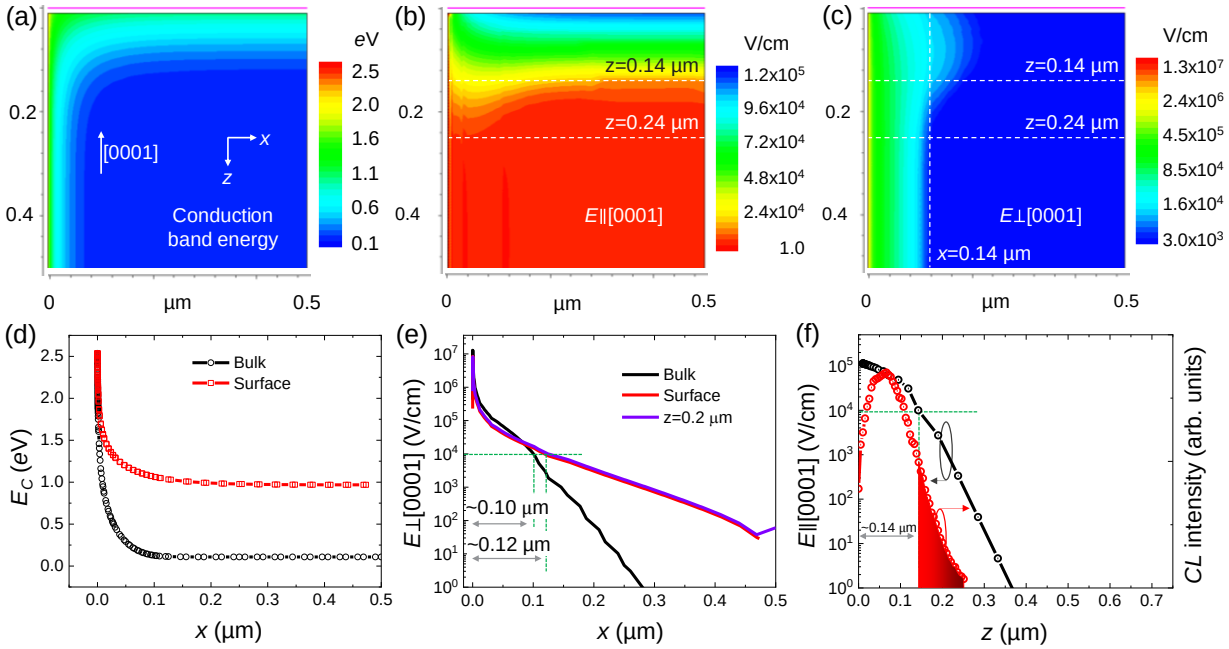

Figure 11: Calculated distribution of (a) conduction band minimum energy E_C and electric field E (b) $E\parallel[0001]$ and (c) $E\perp[0001]$ with dislocation line located at x = 0 along the z-axis and with vacuum/GaN interface at z = 0 µm. (d) Their corresponding E_C profiles in the bulk (z = 0.5 µm) and at the surface (z = 0 µm). (e) $E\perp[0001]$ profiles at z = 0.5 µm, z = 0.2 µm and z = 0 µm. (f) $E\parallel[0001]$ profile away from the dislocation at x = 0.5 µm (left axis) and CL by depth distribution (right axis) obtained from Monte Carlo simulation. And offset is included in *-eCPD* profile for a better clarity.

III. Surface potential analysis

As a positive space charge formed around the *a*- and *a*+*c*-type TDs results in an upward band bending, it is also reflected in the contact potential difference (*CPD*) or in a surface potential measurement by KPFM (see Figure 12b). In the KPFM technique, the *CPD* is measured by nullifying the electrostatic force induced on the metallic tip of the probe by a DC bias (V_{dc}) applied between the probe and the sample. Instead of a static electrostatic force, the dynamic component of the electrostatic force, F_ω, modulating at frequency ω due to an applied bias $V_{ac}\sin(\omega t)$ is measured. This component is generally described as

$$F_\omega = \frac{1}{2}\frac{\partial C}{\partial z}(V_{dc} - CPD)V_{ac}\sin(\omega t) \quad \ldots (7)$$

The *CPD* is generally expressed as follows in terms of the difference of work function between the metallic probe and the sample under investigation

$$\begin{aligned} -e.CPD &= \left(E_{C,surface} - E_F + \chi\right) - \varphi_{metal} \\ &= BB + \left(E_{C,bulk} - E_F + \chi - \varphi_{metal}\right) \quad \ldots (8) \end{aligned}$$

where φ_{metal} is the probe work function, $E_{C,surface}$ and $E_{C,bulk}$, are the conduction band minima at the surface and in the bulk, respectively, E_F, the Fermi-level, χ, the electron affinity and BB, the surface band bending (*BB* is positive if bending is upward) and *e* the elementary charge.

Because the second term in (8) is constant, any variation in the band bending across the surface is proportionally reflected in the change in -*eCPD*. This means, for an upper band bending, the change in -*eCPD* is positive, which should appear with brighter contrast in the -*eCPD* map. Such a map is shown in figure 12(b) where across most of the dislocations, both *a*- and *a*+*c*-type, the upper band bending can be confirmed. It is worth noting that the in-plane band bending (or equivalently potential variation) deduced by this method differs significantly from the electrostatic potential profiles obtained from electron holography as done for across *a*-type TDs by Cherns et al. [18]. The former is sensitive only to the surface/near-surface region, thus impacted by the

surface depletion, while the latter probes the average potential in the bulk and at the surface. The CPD difference between the TDs and the background is found in the range of ~0.09 V– 0.15 V (see Fig. 12c). However, quantitatively this value is significantly smaller than the calculated band bending of ~2.42 *e*V in the bulk (Figure 11a, d) and ~ 1.56 *e*V near the surface (Figure 11d). The latter, which accounts for the charged surface states, is 10 - 17 times larger than the measured - *eCPD*. A similar or even smaller magnitude of *CPD* difference has been previously reported for TDs [8,19,45,46]. Even though equations (7) and (8) are often used to interpret *CPD* for a parallel plate capacitor configuration of a tip-sample system, they cannot be simply extended to the case when charged defects are present as is the case here for charged dislocations. One needs to incorporate the potential induced on the tip by the dislocation line charge and the space charge around it. Rosenwaks et al. [47] calculated the *CPD* for a similar case. They have shown that the *CPD* change across a sub-surface single charged defect in *n*-type semiconductor coincides with the band bending or surface potential only for a zero tip-sample surface distance, and it tends to diminish significantly with increasing tip-sample distance. In their calculation, the *CPD* difference already dropped to 60% of the surface potential at a tip-sample distance of only 1 nm. So, in our case where the tip-sample distance is ~10-12 nm it is not surprising that KPFM is showing a small *CPD* change across charged dislocations. To showcase this, we additionally carried out a TCAD simulation of a metal sphere (radius = 25 nm) separated by 10 nm from the GaN (0001) surface with and without a dislocation. The electric field on the metallic sphere was calculated for varying bias. This was to determine the *CPD* value at which the electric field on the metallic sphere is nullified. Two cases of dislocation were considered: with an electron trap density of (1) 1 e/unit cell and (2) 0.25 e/unit cell. As shown in figure 8b, a *CPD* difference of 0.8 V is expected for the first case, while 0.3 V for the second case. The latter comes close to our experimental value. In our

KPFM experiments, the charging effect was also observed due to this low doping of the GaN layer, which further contributed to a weaker contrast in the -*eCPD* map. This charging effect was confirmed as the CPD contrast continued to become weaker with consecutive KPFM scans of the same area.

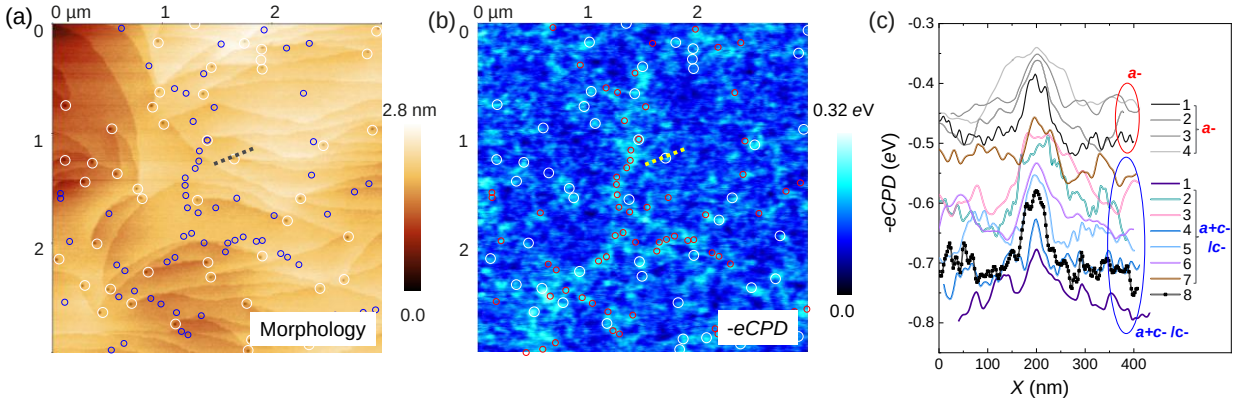

Figure 12: (a) Morphology and the corresponding (b) -*eCPD* maps on *n*-GaN (0001) surface, respectively. *a*-type and *a*+*c*/*c*-type TDs are enclosed in smaller and bigger circles, respectively. (c) -*e*CPD line profiles across 4 *a*-type TDs (marked as *a*- 1, 2, 3, 4) and 8 *a*+*c*-type or *c*- type TDs (marked as *a*+*c*-/*c*- 1, 2, 3...8). The latter are described here as *a*+*c*- or *c*-type as it is not possible to distinguish the two types by mere morphology. All the curves have been shifted along the y-axis by an offset for clarity.

IV. CONCLUSIONS

We carried out a comprehensive study of *a*-type with 5/7 atom-core structure and *a*+*c*-type TDs with 5/6 double (undissociated) and 5/7/4/8/9 atom-core structures (dissociated) in *n*-type GaN (0001) by independently probing the space-charge capacitance, recombination properties,

conductivity, and surface potential around them by different techniques: SCM, CL microscopy, C-AFM and KPFM. Correlative CL and ECCI analysis confirm both types of TDs as non-radiative. To understand this, a cut-off field of ~ 10^4 V/cm was used to borderline the non-radiative region where the exciton dissociation can take place instantly. Because of the polarization discontinuity alone at the site of dislocation termination on surface, this region is confined within ~140 nm in depth from the surface and ~112 nm radially from the dislocation core. Even in dislocation-free zones, for the given band bending the field of the surface depletion region is sufficiently high for exciton dissociation within ~142 nm in depth. Therefore, at a high electron beam energy (7 k*e*V), the CL contrast observed is mainly caused by the dislocation segments enclosed between the depth of ~ 140 nm and 260 nm. As found in the SCM analysis, diminished |dC/dV| and V_{th} shift of ~ -1.76 V (~ -1.10 V) in dC/dV curves at *a*-type (*a*+*c*-type) TDs (with respect to the reference area) confirm positively charged depletion around them. TCAD calculation revealed that these V_{th} shifts correspond to trap density of ~0.25-0.5 *e*/*u.c.* and ~0.25 *e*/*u.c.* for *a*- and *a*+*c*-type dislocations, respectively, with their energy level lying below the mid-gap. These findings also explain the small surface potential variation usually measured across TDs in KPFM measurements. With the charges trapped at dislocations, the cut-off condition for non-radiative recombination is satisfied in their surroundings within 120 nm from their core, which agrees well with the FWHM of the CL dark spots. Coherently, it is confirmed in C-AFM analysis that depletion around TDs inhibits local conduction, which must be considered while estimating device area or carrier concentration from capacitance-based measurement. As direct access to TDs is not readily available in fully fabricated devices, our correlated SCM-ECCI analysis on the cross-sectional surfaces of the diodes could potentially be a more advantageous approach, as it benefits from the absence of polarization effects and allows access to depth information as well. Our cross-sectional analysis on *p*-*n* diodes shows

a good agreement between the electrical characteristics obtained on the entire dislocation segment in the *n*-type drift layer and that assessed from multiple characterization techniques on a (0001) surface.

ACKNOWLEDGEMENTS

Authors would like to thank H. Hahn, M. Marx, R. Oligschlaeger, D. Fahle and M. Heuken, in AIXTRON SE for the epitaxial growth on the engineered QST® substrates.

The project has received funding from the European Union's Horizon 2020 research and innovation programme under the Marie Sklodowska-Curie grant agreement No 896390.

This project has received funding from the ECSEL Joint Undertaking (JU) under grant agreement No 826392. The JU receives support from the European Union's Horizon 2020 research and innovation program and Austria, Belgium, Germany, Italy, Slovakia, Spain, Sweden, Norway, Switzerland.

REFERENCES

[1] H. Amano, Y. Baines, E. Beam, M. Borga, T. Bouchet, R. Chu, C. De Santi, M. M. De Souza, S. Decoutere, L. D. Cioccio, E. Bernd, T. Egawa, P. Fay, J. J. Freedsman, L. Guido, O. Häberlen, G. Haynes, T. Heckel, D. Hemakumara, P. Houston, J. Hu, M. Hua, Q. Huang, A. Huang, S. Jiang, H. Kawai, D. Kinzer, M. Kuball, A. Kumar, K. B. Lee, X. Li, D. Marcon, M. März, R. McCarthy, G. Meneghesso, M. Meneghini, E. Morvan, A. Nakajima, E. M. S. Narayanan, S. Oliver, T. Palacios, D. Piedra, M. Plissonnier, R. Reddy, M. Sun, I. Thayne, A. Torres, N. Trivellin, V. Unni, M. J. Uren, M. Van Hove, D. J. Wallis, J. Wang, J. Xie, S. Yagi, S. Yang, C. Youtsey, R. Yu, E. Zanoni, S. Zeltner, and Y. Zhang, The 2018

GaN power electronics roadmap, J. Phys. D. Appl. Phys. **51**, 163001 (2018).

[2] Y. Zhang, M. Sun, D. Piedra, J. Hu, Z. Liu, Y. Lin, X. Gao, K. Shepard, and T. Palacios, 1200 V GaN Vertical Fin Power Field-Effect Transistors, IEEE Int. Electron Devices Meet. 9.2.1 (2017).

[3] R. Chu, A. Corrion, M. Chen, R. Li, D. Wong, D. Zehnder, B. Hughes, and K. Boutros, 1200-V Normally Off GaN-on-Si Field-Effect Transistors With Low Dynamic ON-Resistance, IEEE Electron Device Lett. **32**, 632 (2011).

[4] Y. Wang, G. Lyu, J. Wei, Z. Zheng, J. Lei, W. Song, L. Zhang, M. Hua, and K. J. Chen, A 1200-V GaN/SiC cascode device with E-mode p-GaN gate HEMT and D-mode SiC junction field-effect transistor, Appl. Phys. Express **12**, 106505 (2019).

[5] J. W. P. Hsu, M. J. Manfra, D. V. Lang, S. Richter, S. N. G. Chu, A. M. Sergent, R. N. Kleiman, and L. N. Pfeiffer, Inhomogeneous spatial distribution of reverse bias leakage in GaN Schottky diodes, Appl. Phys. Lett. **78**, 1685 (2001).

[6] B. Kim, D. Moon, K. Joo, S. Oh, Y. K. Lee, Y. Park, Y. Nanishi, and E. Yoon, Investigation of leakage current paths in n-GaN by conductive atomic force microscopy, Appl. Phys. Lett. **104**, 102101 (2014).

[7] J. W. P. Hsu, M. J. Manfra, S. N. G. Chu, C. H. Chen, L. N. Pfeiffer, and R. J. Molnar, Effect of growth stoichiometry on the electrical activity of screw dislocations in GaN films grown by molecular-beam epitaxy, Appl. Phys. Lett. **78**, 3980 (2001).

[8] J. W. P. Hsu, H. M. Ng, A. M. Sergent, and S. N. G. Chu, Scanning Kelvin force microscopy imaging of surface potential variations near threading dislocations in GaN, Appl. Phys. Lett. **81**, 3579 (2002).

[9] T. Narita, M. Kanechika, J. Kojima, H. Watanabe, T. Kondo, T. Uesugi, S. Yamaguchi, Y. Kimoto, K. Tomita, Y. Nagasato, S. Ikeda, M. Kosaki, T. Oka, and J. Suda, Identification of type of threading dislocation causing reverse leakage in GaN p-n junctions after continuous forward current stress, Sci. Rep. **12**, 1458 (2022).

[10] S. Usami, Y. Ando, A. Tanaka, K. Nagamatsu, M. Deki, M. Kushimoto, S. Nitta, Y. Honda, H. Amano, Y. Sugawara, Y.-Z. Yao, and Y. Ishikawa, Correlation between dislocations and leakage current of p-n diodes on a free-standing GaN substrate, Appl. Phys. Lett. **112**, 182106 (2018).

[11] S. Usami, R. Miyagoshi, A. Tanaka, K. Nagamatsu, M. Kushimoto, M. Deki, S. Nitta, Y.

Honda, and H. Amano, Effect of dislocations on the growth of p-type GaN and on the characteristics of p-n diodes, Phys. Status Solidi Appl. Mater. Sci. **214**, 1600837 (2017).

[12] K. K. Sabelfeld, V. M. Kaganer, C. Pfüller, and O. Brandt, Dislocation contrast in cathodoluminescence and electron-beam induced current maps on GaN(0001), J. Phys. D. Appl. Phys. **50**, 405101 (2017).

[13] M. Albrecht, J. L. Weyher, B. Lucznik, I. Grzegory, and S. Porowski, Nonradiative recombination at threading dislocations in n-type GaN: Studied by cathodoluminescence and defect selective etching, Appl. Phys. Lett. **92**, 231909 (2008).

[14] Y. Yao, Y. Ishikawa, M. Sudo, Y. Sugawara, and D. Yokoe, Characterization of threading dislocations in GaN (0001) substrates by photoluminescence imaging, cathodoluminescence mapping and etch pits, J. Cryst. Growth **468**, 484 (2017).

[15] G. Naresh-Kumar, J. Bruckbauer, P. R. Edwards, S. Kraeusel, B. Hourahine, R. W. Martin, M. J. Kappers, M. A. Moram, S. Lovelock, R. A. Oliver, C. J. Humphreys, and C. Trager-Cowan, Coincident electron channeling and cathodoluminescence studies of threading dislocations in GaN, Microsc. Microanal. **20**, 55 (2014).

[16] T. Tanikawa, K. Ohnishi, M. Kanoh, T. Mukai, and T. Matsuoka, Three-dimensional imaging of threading dislocations in GaN crystals using two-photon excitation photoluminescence, Appl. Phys. Express **11**, 031004 (2018).

[17] V. M. Kaganer, K. K. Sabelfeld, and O. Brandt, Piezoelectric field, exciton lifetime, and cathodoluminescence intensity at threading dislocations in GaN (0001), Appl. Phys. Lett. **112**, 122101 (2018).

[18] D. Cherns and C. G. Jiao, Electron holography studies of the charge on dislocations in GaN, Phys. Rev. Lett. **87**, 205504 (2001).

[19] B. S. Simpkins, E. T. Yu, P. Waltereit, and J. S. Speck, Correlated scanning Kelvin probe and conductive atomic force microscopy studies of dislocations in gallium nitride, J. Appl. Phys. **94**, 1448 (2003).

[20] E. Secco, A. Minj, N. Garro, A. Cantarero, J. Colchero, A. Urban, C. I. Oppo, J. Malindretos, and A. Rizzi, Structural characterization of selective area growth GaN nanowires by non-destructive optical and electrical techniques, J. Phys. D. Appl. Phys. **48**, 305301 (2015).

[21] P. J. Hansen, Y. E. Strausser, A. N. Erickson, E. J. Tarsa, P. Kozodoy, E. G. Brazel, J. P.

Ibbetson, U. Mishra, V. Narayanamurti, S. P. DenBaars, and J. S. Speck, Scanning capacitance microscopy imaging of threading dislocations in GaN films grown on (0001) sapphire by metalorganic chemical vapor deposition, Appl. Phys. Lett. **72**, 2247 (1998).

[22] A. Szyszka, M. Wośko, B. Paszkiewicz, and R. Paszkiewicz, Surface electrical characterization of defect related inhomogeneities of AlGaN/GaN/Si heterostructures using scanning capacitance microscopy, Mater. Sci. Semicond. Process. **94**, 57 (2019).

[23] D. M. Schaadt, E. J. Miller, E. T. Yu, and J. M. Redwing, Lateral variations in threshold voltage of an $Al_xGa_{1-x}N$/GaN heterostructure field-effect transistor measured by scanning capacitance spectroscopy, Appl. Phys. Lett. **78**, 88 (2001).

[24] P. Ebert, L. Ivanova, S. Borisova, H. Eisele, A. Laubsch, and M. Dähne, Electronic properties of dislocations in GaN investigated by scanning tunneling microscopy, Appl. Phys. Lett. **94**, 062104 (2009).

[25] P. H. Weidlich, M. Schnedler, H. Eisele, R. E. Dunin-Borkowski, and P. Ebert, Repulsive interactions between dislocations and overgrown v-shaped defects in epitaxial GaN layers, Appl. Phys. Lett. **103**, 142105 (2013).

[26] V. Odnoblyudov, C. Basceri, and S. Farrens, Engineered substrate structure for power and RF applications, United States Pat. 15/621,335 (2018).

[27] A. Minj, M. Zhao, B. Bakeroot, and K. Paredis, Imaging confined and bulk p-type/n-type carriers in (Al,Ga)N heterostructures with multiple quantum wells, Appl. Phys. Lett. **118**, 032104 (2021).

[28] H. Han, T. Hantschel, A. Schulze, L. Strakos, T. Vystavel, R. Loo, B. Kunert, R. Langer, W. Vandervorst, and M. Caymax, Enhancing the defect contrast in ECCI through angular filtering of BSEs, Ultramicroscopy **210**, 112922 (2020).

[29] M. Lamhamdi, F. Cayrel, E. Frayssinet, A. E. Bazin, A. Yvon, E. Collard, Y. Cordier, and D. Alquier, Two-dimensional dopant profiling of gallium nitride p-n junctions by scanning capacitance microscopy, Nucl. Instruments Methods Phys. Res. Sect. B Beam Interact. with Mater. Atoms **372**, 67 (2016).

[30] F. Giannazzo, F. Iucolano, F. Roccaforte, L. Romano, M. G. Grimaldi, and V. Raineri, Electrical activation and carrier compensation in Si and Mg implanted GaN by scanning capacitance microscopy, Solid State Phenom. **131**–**133**, 491 (2008).

[31] J. Sumner, R. A. Oliver, M. J. Kappers, and C. J. Humphreys, Assessment of the

performance of scanning capacitance microscopy for n-type gallium nitride, J. Vac. Sci. Technol. B Microelectron. Nanom. Struct. **26**, 611 (2008).

[32] N. Duhayon, P. Eyben, M. Fouchier, T. Clarysse, W. Vandervorst, D. Álvarez, S. Schoemann, M. Ciappa, M. Stangoni, W. Fichtner, P. Formanek, M. Kittler, V. Raineri, F. Giannazzo, D. Goghero, Y. Rosenwaks, R. Shikler, S. Saraf, S. Sadewasser, N. Barreau, T. Glatzel, M. Verheijen, S. A. M. Mentink, M. von Sprekelsen, T. Maltezopoulos, R. Wiesendanger, and L. Hellemans, Assessing the performance of two dimensional dopant profiling techniques, J. Vac. Sci. Technol. B **22**, 385 (2003).

[33] See Supplemental Material at for a brief description of chemical analysis by TOF-SIMS, |dC/dV| versus doping concentration on calibration structure T8/3, STEM analysis for the identification of the dislocation core-structures, and valence band spectra

[34] C. S. Jiang, J. T. Heath, H. R. Moutinho, and M. M. Al-Jassim, Scanning capacitance spectroscopy on *n*+-*p* asymmetrical junctions in multicrystalline Si solar cells, J. Appl. Phys. **110**, 014514 (2011).

[35] K. S. Qwah, C. A. Robertson, Y. Wu, and J. S. Speck, Modeling dislocation-related reverse bias leakage in GaN *p*-*n* diodes, Semicond. Sci. Technol. **36**, 075001 (2021).

[36] E. Baghani and S. K. O'Leary, Dislocation line charge screening within *n*-type gallium nitride, J. Appl. Phys. **113**, 023709 (2013).

[37] E. Baghani and S. K. O'Leary, Occupation statistics of dislocations within uncompensated *n*-type wurtzite gallium nitride, J. Appl. Phys. **109**, 113706 (2011).

[38] S. L. Rhode, M. K. Horton, W. Y. Fu, S. L. Sahonta, M. J. Kappers, T. J. Pennycook, C. J. Humphreys, R. O. Dusane, and M. A. Moram, Dislocation core structures in Si-doped GaN, Appl. Phys. Lett. **107**, 243104 (2015).

[39] I. Belabbas, J. Chen, and G. Nouet, Electronic structure and metallization effects at threading dislocation cores in GaN, Comput. Mater. Sci. **90**, 71 (2014).

[40] A. Lochthofen, W. Mertin, G. Bacher, L. Hoeppel, S. Bader, J. Off, and B. Hahn, Electrical investigation of V-defects in GaN using Kelvin probe and conductive atomic force microscopy, Appl. Phys. Lett. **93**, 022107 (2008).

[41] S. Besendörfer, E. Meissner, A. Lesnik, J. Friedrich, A. Dadgar, and T. Erlbacher, Methodology for the investigation of threading dislocations as a source of vertical leakage in AlGaN/GaN-HEMT heterostructures for power devices, J. Appl. Phys. **125**, 095704

(2019).

[42] S. F. Chichibu, K. Shima, K. Kojima, S. Y. Takashima, K. Ueno, M. Edo, H. Iguchi, T. Narita, K. Kataoka, S. Ishibashi, and A. Uedono, Room temperature photoluminescence lifetime for the near-band-edge emission of epitaxial and ion-implanted GaN on GaN structures, Jpn. J. Appl. Phys. **58**, SC0802 (2019).

[43] S. F. Chichibu, A. Uedono, T. Onuma, B. A. Haskell, A. Chakraborty, T. Koyama, P. T. Fini, S. Keller, S. P. Denbaars, J. S. Speck, U. K. Mishra, S. Nakamura, S. Yamaguchi, S. Kamiyama, H. Amano, I. Akasaki, J. Han, and T. Sota, Origin of defect-insensitive emission probability in In-containing (Al,In,Ga)N alloy semiconductors, Nat. Mater. **5**, 810 (2006).

[44] J. P. Ibbetson, P. T. Fini, K. D. Ness, S. P. Denbaars, J. S. Speck, and U. K. Mishra, Polarization effects, surface states, and the source of electrons in AlGaN/GaN heterostructure field effect transistors, Appl. Phys. Lett. **77**, 250 (2000).

[45] G. Koley and M. G. Spencer, Scanning Kelvin probe microscopy characterization of dislocations in III-nitrides grown by metalorganic chemical vapor deposition, Appl. Phys. Lett. **78**, 2873 (2001).

[46] A. Minj, D. Cavalcoli, G. R. Mutta Popuri, A. Vilalta-Clemente, P. Ruterana, and A. Cavallini, Electrical properties of extended defects in III-nitrides, Acta Mater. **89**, 290 (2015).

[47] Y. Rosenwaks, R. Shikler, T. Glatzel, and S. Sadewasser, Kelvin probe force microscopy of semiconductor surface defects, Phys. Rev. B **70**, 085320 (2004).